

Spin phase detection by spin current in a chiral helimagnet

Nan Jiang^{†,1,2,3,*} Shota Suzuki^{†,1} Issei Sasaki^{†,1} Kazuki Yamada,¹ Ryoma Kawahara,¹ Shintaro Takada,^{1,3,4} Yusuke Shimamoto,⁵ Hiroki Shoji,⁵ Yusuke Kousaka,⁵ Jun-ichiro Ohe,⁶ Yoshihiko Togawa,⁵ and Yasuhiro Niimi^{1,2,3}

¹*Department of Physics, Graduate School of Science,
Osaka University, Toyonaka, Osaka 560-0043, Japan*

²*Center for Spintronics Research Network, Osaka University, Toyonaka 560-8531, Japan*

³*Institute for Open and Transdisciplinary Research Initiatives, Osaka University, Suita 565-0871, Japan*

⁴*Center for Quantum Information and Quantum Biology, Osaka University, Toyonaka 560-0043, Japan*

⁵*Department of Physics and Electronics, Osaka Metropolitan University, Sakai, Osaka 599-8531, Japan*

⁶*Department of Physics, Toho University, Funabashi, Chiba 274-8510, Japan*

(Dated: June 14, 2025)

Helimagnets, characterized by a helical arrangement of magnetic moments, possess unique internal degrees of freedom, including the spin phase, defined by the phase of the helical magnetic structure. Electrical detection of the spin phase is essential for both practical applications and fundamental research in helimagnets. Here, we demonstrate the electrical detection of the spin phase in a van der Waals nanoscale chiral helimagnet CrNb_3S_6 using nonlocal spin valve measurements. Due to the short spin diffusion length in CrNb_3S_6 (~ 5 nm), the surface magnetic moment direction, which corresponds to the spin phase, can be detected via spin currents. The experimentally observed magnetic field dependence of the nonlocal spin valve signal is consistent with that of the surface magnetic moment in the helical magnetic structure, as supported by micromagnetic simulations. Our results establish spin currents as a powerful tool for detecting the spin phase in helimagnets, opening avenues for utilizing the spin phase as a novel internal degree of freedom in nanoscale spintronic devices.

Phase is a fundamental concept in condensed matter physics, underlying phenomena such as charge density waves, Wigner crystals, Josephson junctions, and qubits. In magnetism, helimagnets [1–8], with their helical spin arrangements, provide a unique platform where phase plays a central role. Unlike ferromagnets and antiferromagnets, helimagnets have two internal degrees of freedom: helicity and spin phase. Helicity indicates the rotational handedness of the spin texture (right- or left-handed), while the spin phase (see Fig. 1a) specifies the position within the helical cycle. This duality gives helimagnets richer tunability, enabling novel spintronic applications.

In centrosymmetric helimagnets [1–4], helicity can be controlled by electric currents under a magnetic field [9–11] and electrically detected through nonreciprocal transport [9, 11] or current-induced spin accumulation [11]. In contrast, in noncentrosymmetric helimagnets [5–8], such as chiral helimagnets, the helicity is fixed by the crystal structure and cannot be externally manipulated, although it remains electrically detectable [12–14]. This makes the spin phase the primary internal degree of freedom.

In nanoscale chiral helimagnets, the spin phase directly corresponds to the surface magnetic moment orientation, as illustrated in Fig. 1a. While surface-sensitive techniques such as x-ray magnetic circular dichroism [15–18] and spin-polarized scanning tunneling microscopy [19–21] can probe surface magnetization, their reliance on ultra-high vacuum or synchrotron radiation severely limits practical applications. Conventional electrical detection of magnetization, such as anomalous Hall effect mea-

surements [22], can detect only the net magnetization averaged over the conducting region, making it impossible to isolate surface contributions. Thus, an electrical method to detect the spin phase is crucial for practical devices.

Spin currents offer a promising alternative for detecting spin states in magnetic materials [23]. In these materials, the spin diffusion length, that is the characteristic distance over which a spin current decays, is typically on the order of a few nanometers. As a result, injected spin currents mainly interact with surface magnetic moments. This inherent surface sensitivity makes spin currents ideal for probing the spin phase in nanoscale helimagnets. Furthermore, nonlocal spin valve (NLSV) devices utilizing spin currents [24–29] provide a sensitive platform for detecting magnetization directions and spin fluctuations [30–34], enabling novel spintronic applications.

Here, we demonstrate electrical spin phase detection in a nanoscale helimagnet using spin currents. As a simple yet effective platform, we focus on a van der Waals (vdW) chiral helimagnet CrNb_3S_6 , which possesses only one helicity. Using a NLSV device with CrNb_3S_6 , we successfully detect the spin phase in nanoscale chiral helimagnets, supported by micromagnetic simulations. Additionally, inverse spin Hall effect (ISHE) measurements reveal spin fluctuations in chiral helimagnets, opening a route to studying chiral spin dynamics. Our results establish spin currents as a powerful probe for both electrical spin phase detection and spin fluctuation analysis, highlighting the spin phase as a key degree of freedom in nanoscale spintronics.

SPIN CURRENT DEVICE WITH A CHIRAL HELIMAGNET

CrNb_3S_6 [35–48] is a chiral helimagnet with a non-centrosymmetric crystal structure belonging to the space group $P6_322$. It consists of hexagonal NbS_2 planes with Cr atoms intercalated at one-third of the vdW gaps, as illustrated in Fig. 1b. Due to the Dzyaloshinskii-Moriya (DM) interaction, CrNb_3S_6 exhibits a helical magnetic phase below $T_C \sim 130$ K [48]. The helical axis runs along the c -axis, forming a chiral soliton lattice under an in-plane magnetic field [42]. CrNb_3S_6 can be cleaved along the helical axis using mechanical exfoliation, achieving thicknesses of several tens of nanometers [49].

To detect the spin phase via spin currents, we fabricated a lateral spin valve with insertion of a CrNb_3S_6 flake between two permalloy (Py) wires, all connected by a Cu wire (Fig. 1c). The thickness t of the CrNb_3S_6 thin flakes used in this work can be classified into two types: one with a thickness approximately equal to the length of one helical period of CrNb_3S_6 ($L_0 (= 48 \text{ nm})$) under zero magnetic field [39, 42], and the other with a thickness approximately equal to $1.5L_0$. These values are confirmed via atomic force microscopy and magnetoresistance measurements. Figures 1d and 1e show the magnetoresistances of CrNb_3S_6 thin flakes with $t = 43 \text{ nm}$ ($\approx L_0$) and $t = 72 \text{ nm}$ ($\approx 1.5L_0$), respectively. For $t \approx 1.5L_0$, a sudden jump and hysteresis appear due to changes in the number of magnetic solitons [49], while no such features are observed for $t \approx L_0$.

Before detecting the spin phase with spin current, we evaluate the spin diffusion length in CrNb_3S_6 ($\lambda_{\text{CrNb}_3\text{S}_6}$). We have performed NLSV measurements [24–29] with and without the CrNb_3S_6 thin flake, as illustrated in Figs. 2a and 2b. By applying an electric current I from the left Py wire to the Cu wire, spin accumulation is generated at the interface between Py and Cu, which diffuses along the Cu wire, resulting in a spin current flow. When another Py wire is placed within the spin diffusion length, a nonlocal voltage (V_{NL1}) dependent on the electrochemical potential is detected. When a CrNb_3S_6 flake is inserted as a middle wire (Fig. 2b), a part of the spin current is absorbed into the CrNb_3S_6 flake. As a result, the NLSV signal $\Delta R_{\text{S1}} = \Delta V_{\text{NL1}}/I$ is reduced compared to the signal without the CrNb_3S_6 flake because of the strong spin-orbit interaction of CrNb_3S_6 , as shown in Fig. 2c.

The temperature dependence of ΔR_{S1} for devices with and without the CrNb_3S_6 flake is shown in Extended Data Fig. 1. From the reduction rate, $\Delta R_{\text{S1}}^{\text{with}}/\Delta R_{\text{S1}}^{\text{without}}$, we have obtained $\lambda_{\text{CrNb}_3\text{S}_6}$ using a one-dimensional spin diffusion model [29]. Figure 2d shows $\lambda_{\text{CrNb}_3\text{S}_6}$ as a function of temperature. $\lambda_{\text{CrNb}_3\text{S}_6}$ is approximately 5 nm at low temperatures. It decreases sharply above 50 K and is saturated at 1 nm above T_C . The temperature dependence of the resistance R of the CrNb_3S_6 thin flake is

shown in the inset of Fig. 2d. $\lambda_{\text{CrNb}_3\text{S}_6}$ is nearly inversely proportional to R , indicating that the Elliott-Yafet mechanism [50, 51] is dominant in this material.

DETECTION OF SPIN PHASE BY SPIN CURRENT

Next, we demonstrate spin phase detection using a lateral spin valve consisting of Py and CrNb_3S_6 , as shown in Fig. 3a. In a conventional NLSV with two ferromagnetic wires, the NLSV signal changes the sign, depending on whether the injector and detector magnetizations are parallel or antiparallel. In our setup, we replace the detector Py wire by the chiral helimagnet CrNb_3S_6 flake. Since the spin current in CrNb_3S_6 decays within $\lambda_{\text{CrNb}_3\text{S}_6}$ ($\approx 5 \text{ nm}$) much smaller than the helical period $L_0 (= 48 \text{ nm})$ as discussed in the previous section, it is inherently surface-sensitive, enabling us to probe the surface magnetic moment direction and thus the spin phase.

Figure 3b shows the NLSV signal $R_{\text{S2}} \equiv V_{\text{NL2}}/I$ at low magnetic fields for the $t \approx L_0$ thick CrNb_3S_6 flake. A clear rectangular R_{S2} is observed. As H_y increases from negative values, R_{S2} abruptly switches to negative at 50 Oe and returns to positive at 250 Oe (see the red curve). Similar behavior is observed during the reverse field sweep (see the blue curve). In the present device, the magnetization of the Py wire (left side in Fig. 1c) is known to flip at $H_y \approx 250 \text{ Oe}$ [26], meaning that the jump at $H_y \approx \pm 50 \text{ Oe}$ originates from the CrNb_3S_6 flake. This jump in R_{S2} reflects a sign change in the y -component of the surface magnetic moment, indicating spin phase rotation by 180° .

The 180° spin phase rotation under an external field suggests the existence of a net magnetization, indicating that a helical magnetic structure with a period shorter than L_0 , rather than a perfect one-pitch helical structure, is realized. Magnetic pinning effects likely prevent forming a perfect one-pitch helix in such a thin flake. This interpretation is further supported by the absence of resistance jumps associated with changes in the number of solitons for the $t \approx L_0$ thick CrNb_3S_6 flake (see Fig. 1d).

Figure 3c shows the NLSV signal over a wider magnetic field range for another $t \approx L_0$ thick CrNb_3S_6 flake. Clear jumps in R_{S2} are also observed in this 52 nm thick sample, indicating that a helical structure with a period shorter than one pitch is realized even at this thickness. In addition, R_{S2} exhibits a gradual change from high to low magnetic fields, reflecting the continuous evolution of the surface magnetic moment direction in CrNb_3S_6 . Surface barriers in chiral helimagnets can lead to a chiral surface twist [35, 52–54], causing this gradual rotation of surface magnetic moment direction at higher fields. The expected magnetic structures at characteristic magnetic fields during the magnetic field increasing process for the $t \approx L_0$ thick CrNb_3S_6 flake are illustrated in Fig. 3d. Ad-

ditionally, the magnetoresistance of CrNb_3S_6 may influence R_{S2} through the spin resistance at the $\text{CrNb}_3\text{S}_6/\text{Cu}$ interface [28].

We then examine R_{S2} at low magnetic fields for a $t \approx 1.5L_0$ thick CrNb_3S_6 flake, shown in Fig. 3e. Similar to Fig. 3b, the jumps in R_{S2} at ± 250 Oe originate from the magnetization flip of the Py wire. In the low magnetic field region, on the other hand, R_{S2} behaves differently from the case of $t \approx L_0$: it gradually decreases from -50 Oe (or $+50$ Oe), crosses zero near 0 Oe, becomes negative, and flattens around -100 Oe (or $+100$ Oe) as H_y increases (or decreases) further. This gradual change in R_{S2} at low magnetic fields can be attributed to a continuous change of the y -component of the surface magnetic moment for the $1.5L_0$ helical magnetic structure. The $1.5L_0$ structure has the same net magnetization as a $0.5L_0$ helical structure. In the $0.5L_0$ structure, the surface magnetic moment is perpendicular to the net magnetization at 0 Oe. This leads to $R_{\text{S2}} = 0$ at ≈ 0 Oe. As the magnetic field increases, the surface magnetic moment rotates toward the field direction to increase the net magnetization. This rotation causes the gradual change in R_{S2} . The expected magnetic structures at characteristic low magnetic fields during the magnetic field increasing process for the $t \approx 1.5L_0$ thick CrNb_3S_6 flake are illustrated in Fig. 3g (see states 3-5).

The NLSV signal over a wider magnetic field range for the $t \approx 1.5L_0$ thick CrNb_3S_6 flake is shown in Fig. 3f. When H_y is increased from negative values (see the red data in Fig. 3e), R_{S2} exhibits jumps around -500 Oe and 800 Oe, corresponding to magnetic fields where the number of magnetic solitons changes, as confirmed by the magnetoresistance shown in Fig. 1e. Additionally, R_{S2} gradually decreases from -3000 Oe to -500 Oe, likely due to the continuous evolution of the surface magnetic moment direction caused by the chiral surface twist (state 2 in Fig. 3g). After one magnetic soliton is inserted, the surface magnetic moment aligns parallel to the magnetic field, resulting in a positive R_{S2} once again (state 3 in Fig. 3g). A similar behavior due to the chiral surface twist is also observed after soliton extraction (state 6 in Fig. 3g). Changes in the resistance R of CrNb_3S_6 may also contribute to the variations in R_{S2} . A similar behavior is observed during the opposite field sweep (see the blue data in Fig. 3e).

As discussed in this section, the observed magnetic field dependence of R_{S2} for the $t \approx L_0$ and $t \approx 1.5L_0$ thick CrNb_3S_6 flakes is consistent with the expected behavior of the surface magnetic moment in a chiral helimagnet. These results confirm the successful spin phase detection using spin currents in NLSV devices. This is further corroborated by micromagnetic simulations in the next section. The reproducibility of these findings has been confirmed in different devices, as shown in Extended Data Fig. 2.

MICROMAGNETIC SIMULATIONS

To further verify the magnetic field dependence of R_{S2} , we have calculated magnetic structures for different helical magnetic structure lengths L_z . Details of the simulations are provided in the METHODS section. Since the experimental results indicate that a helical magnetic structure with a period shorter than L_0 , rather than a perfect one-pitch helical structure, is realized in $t \approx L_0$ thick CrNb_3S_6 flakes, we have performed simulations for the $L_z = 7$ ($\approx 0.5L_0$) helical magnetic structure.

Figures 4a shows snapshots of the magnetization components along the x - and y -directions (M_x and M_y , respectively) and magnetic structure averaged over 10 spins at characteristic magnetic fields during the field-increasing process. At $H = -H_0$, which is large enough to prepare a forced ferromagnetic state, all spins align nearly along the magnetic field direction ($-y$ direction) (state 1). As the magnetic field increases, the surface magnetic moments at the edges of the L_z direction begin canting toward the x -axis due to the chiral surface twist (state 2). At a small positive magnetic field, a 180° spin phase rotation occurs (state 3). After this spin phase switching, the surface magnetic moments gradually realign with the magnetic field (state 4).

These behaviors are consistent with the expected magnetic structure for the $t \approx L_0$ thick CrNb_3S_6 flake inferred from the experimental R_{S2} data, as illustrated in Fig. 3d. This confirms that spin currents in NLSV devices can effectively detect the surface magnetic moment, i.e., the spin phase.

To justify the use of $L_z = 7$ ($\approx 0.5L_0$) in our simulations, we have also performed calculations for the $L_z = 14$ ($\approx L_0$) helical magnetic structure, as shown in Extended Data Fig. 3. In this case, the surface magnetic moments rotate toward the $+y$ direction before reaching 0 Oe during the increasing field process (see state2 in Extended Data Fig. 3). As a result, the system forms a complete one-pitch helical structure at 0 Oe. Moreover, no 180° spin phase rotation is observed. This behavior contrasts with the experimental results, supporting our interpretation that the realized magnetic structure has a period shorter than L_0 .

Next, we investigate the $t \approx 1.5L_0$ thick CrNb_3S_6 flake by analyzing the $L_z = 21$ ($\approx 1.5L_0$) helical magnetic structure, as shown in Fig. 4b. As the magnetic field increases from $H = -H_0$ (state 1), the surface magnetic moments rotate toward the $+y$ direction before soliton insertion due to the chiral surface twist (state 2). After the soliton insertion, the surface magnetic moments align along the magnetic field to increase the net magnetization. As a result, they gradually rotate from the $-y$ to the $+y$ direction (states 3-5). The surface twisted configuration immediately after soliton extraction, shown as state 6 in Fig. 3g, does not appear in our simulations.

This is because the soliton still remains even at higher magnetic fields (state 6' in Fig. 4b). The larger soliton extraction field in the simulation compared to the experiment could be due to differences in physical parameters such as temperature and the number of spins between the two cases [55].

These behaviors, except for state 6, closely resemble the expected magnetic structures for the $t \approx 1.5L_0$ thick CrNb_3S_6 flake, as inferred from the experimental $R_{\text{S}2}$ data and illustrated in Fig. 3g. This further confirms spin currents effectively detect the surface moment, i.e., the spin phase.

SPIN HALL EFFECT

To investigate spin fluctuations in chiral helimagnets [13], we have measured the ISHE in CrNb_3S_6 flakes using the spin absorption method, as illustrated in Fig. 5a. By applying a current I from the left Py wire to the Cu wire, part of the spin current is injected into CrNb_3S_6 . When the Py magnetization is fully polarized along the Cu wire ($|H_x| > 3000$ Oe), spin-to-charge conversion via the ISHE occurs in CrNb_3S_6 .

Figure 5b shows the ISHE signals of the 72 nm-thick CrNb_3S_6 device measured at $T = 130$ K and 300 K. The ISHE resistance, R_{ISHE} , is defined as the detected voltage drop V_{ISHE} along the CrNb_3S_6 flake divided by I . When $|H_x| > 3000$ Oe, R_{ISHE} saturates. At room temperature, a clear negative ISHE signal [$2\Delta R_{\text{ISHE}} \equiv R_{\text{ISHE}}(H_x > 3000 \text{ Oe}) - R_{\text{ISHE}}(H_x < -3000 \text{ Oe})$] is observed, consistent with the behavior of pure Nb [27]. However, near the critical temperature $T_C = 130$ K, the ISHE signal reverses its sign, becoming positive.

Figure 5c shows the temperature dependence of ΔR_{ISHE} for CrNb_3S_6 devices with two different thicknesses. We also estimated the spin Hall angle, α_H , assuming an interface shunting factor of approximately 0.2 between Cu and CrNb_3S_6 [27], as shown in Fig. 5d. For both devices, ΔR_{ISHE} and α_H peak at $T_C = 130$ K. The sign of ΔR_{ISHE} and α_H remains negative for the 43 nm-thick CrNb_3S_6 device, whereas a sign reversal occurs near T_C for the 72 nm-thick device. Reproducibility across other devices is demonstrated in Extended Data Fig. 4. These results suggest that magnetic fluctuations near T_C lead to the ISHE sign reversal in the thicker device.

Since a full helical pitch isn't realized in the 43nm flake, as discussed in previous sections, the observed magnetic fluctuations may be associated with helical magnetic ordering. Similar behavior around the critical temperature has been reported in ferromagnets [30–32] and antiferromagnets [33], where magnetic fluctuations play a significant role [34]. While magnetic fluctuations are also expected in our case, further studies are needed to elucidate their precise role.

Before closing this section, we address the potential in-

fluence of thermoelectric signals in ISHE measurements with a lateral spin valve structure, particularly in magnetic materials [56]. Heat currents at the spin injection interface can generate voltages at the detection interface through the anomalous Nernst effect in addition to the ISHE. However, the temperature dependence of ΔR_{ISHE} in our measurements does not follow that of the CrNb_3S_6 magnetization [39], excluding thermoelectric effects as a dominant contribution to R_{ISHE} .

CONCLUSION

In conclusion, we have demonstrated the spin phase detection in a vdW nanoscale chiral helimagnet CrNb_3S_6 using NLSV devices. Due to its short spin diffusion length (≈ 5 nm), we successfully detected the surface magnetic moment direction, corresponding to the spin phase. NLSV measurements on CrNb_3S_6 flakes with thicknesses of nearly L_0 and $1.5L_0$ have revealed a non-monotonic magnetic field dependence of spin signal, consistent with the field-dependent behavior of the surface magnetic moment in $0.5L_0$ and $1.5L_0$ helical magnetic structures, as supported by micromagnetic simulations. Furthermore, ISHE measurements have detected a sign change in the spin Hall angle near T_C , attributed to spin fluctuations in the chiral helimagnet. These results establish spin currents as a powerful probe for spin phase and fluctuations, demonstrating their nanoscale effectiveness. Moreover, our findings highlight the spin phase as a key internal degree of freedom in nanoscale spintronic devices, paving the way for new research directions in spintronics.

* nan.jiang@phys.sci.osaka-u.ac.jp; † These authors contributed equally to this work.

- [1] A. Yoshimori, A New Type of Antiferromagnetic Structure in the Rutile Type Crystal, *Journal of the Physical Society of Japan* **14**, 807 (1959).
- [2] T. A. Kaplan, Classical Spin-Configuration Stability in the Presence of Competing Exchange Forces, *Phys. Rev.* **116**, 888 (1959).
- [3] J. Villain, La structure des substances magnetiques, *Journal of Physics and Chemistry of Solids* **11**, 303 (1959).
- [4] T. Nagamiya, Helical Spin Ordering—1 Theory of Helical Spin Configurations (Academic Press, 1968) pp. 305–411.
- [5] I. Dzyaloshinsky, A thermodynamic theory of “weak” ferromagnetism of antiferromagnetics, *Journal of Physics and Chemistry of Solids* **4**, 241 (1958).
- [6] I. Dzyaloshinskii, Theory of helicoidal structures in antiferromagnets. I. Nonmetals, *Sov. Phys. JETP* **19**, 960 (1964).
- [7] I. Dzyaloshinskii, The theory of helicoidal structures in antiferromagnets. II. metals, *Sov. Phys. JETP* **20**, 223 (1965).

- [8] T. Moriya, Anisotropic superexchange interaction and weak ferromagnetism, *Physical review* **120**, 91 (1960).
- [9] N. Jiang, Y. Nii, H. Arisawa, E. Saitoh, and Y. Onose, Electric current control of spin helicity in an itinerant helimagnet, *Nature Communications* **11**, 1601 (2020).
- [10] J.-i. Ohe and Y. Onose, Chirality control of the spin structure in monoaxial helimagnets by charge current, *Applied Physics Letters* **118**, 042407 (2021).
- [11] H. Masuda, T. Seki, J.-i. Ohe, Y. Nii, H. Masuda, K. Takanashi, and Y. Onose, Room temperature chirality switching and detection in a helimagnetic MnAu₂ thin film, *Nature Communications* **15**, 1999 (2024).
- [12] T. Yokouchi, N. Kanazawa, A. Kikkawa, D. Morikawa, K. Shibata, T. Arima, Y. Taguchi, F. Kagawa, and Y. Tokura, Electrical magnetochiral effect induced by chiral spin fluctuations, *Nature Communications* **8**, 866 (2017).
- [13] R. Aoki, Y. Kousaka, and Y. Togawa, Anomalous Nonreciprocal Electrical Transport on Chiral Magnetic Order, *Phys. Rev. Lett.* **122**, 057206 (2019).
- [14] A. Inui, R. Aoki, Y. Nishiue, K. Shiota, Y. Kousaka, H. Shishido, D. Hirobe, M. Suda, J.-i. Ohe, J.-i. Kishine, H. M. Yamamoto, and Y. Togawa, Chirality-Induced Spin-Polarized State of a Chiral Crystal CrNb₃S₆, *Phys. Rev. Lett.* **124**, 166602 (2020).
- [15] J. Stöhr, X-ray magnetic circular dichroism spectroscopy of transition metal thin films, *Journal of Electron Spectroscopy and Related Phenomena* **75**, 253 (1995), future Perspectives for Electron Spectroscopy with Synchrotron Radiation.
- [16] T. Funk, A. Deb, S. J. George, H. Wang, and S. P. Cramer, X-ray magnetic circular dichroism—a high energy probe of magnetic properties, *Coordination Chemistry Reviews* **249**, 3 (2005).
- [17] A. Rogalev, F. Wilhelm, N. Jaouen, J. Goulon, and J.-P. Kappler, X-ray magnetic circular dichroism: Historical perspective and recent highlights, in *Magnetism: A Synchrotron Radiation Approach*, edited by E. Beaupaire, H. Bulou, F. Scheurer, and J.-P. Kappler (Springer Berlin Heidelberg, Berlin, Heidelberg, 2006) pp. 71–93.
- [18] G. van der Laan and A. I. Figueroa, X-ray magnetic circular dichroism—a versatile tool to study magnetism, *Coordination Chemistry Reviews* **277–278**, 95 (2014).
- [19] M. Bode, Spin-polarized scanning tunnelling microscopy, *Reports on Progress in Physics* **66**, 523 (2003).
- [20] M. Bode, M. Heide, K. von Bergmann, P. Ferriani, S. Heinze, G. Bihlmayer, A. Kubetzka, O. Pietzsch, S. Blügel, and R. Wiesendanger, Chiral magnetic order at surfaces driven by inversion asymmetry, *Nature* **447**, 190 (2007).
- [21] R. Wiesendanger, Spin mapping at the nanoscale and atomic scale, *Rev. Mod. Phys.* **81**, 1495 (2009).
- [22] N. Nagaosa, J. Sinova, S. Onoda, A. H. MacDonald, and N. P. Ong, Anomalous hall effect, *Reviews of modern physics* **82**, 1539 (2010).
- [23] W. Han, S. Maekawa, and X.-C. Xie, Spin current as a probe of quantum materials, *Nature materials* **19**, 139 (2020).
- [24] F. J. Jedema, H. B. Heersche, A. T. Filip, J. J. A. Baselmans, and B. J. van Wees, Electrical detection of spin precession in a metallic mesoscopic spin valve, *Nature* **416**, 713 (2002).
- [25] L. Vila, T. Kimura, and Y. Otani, Evolution of the Spin Hall Effect in Pt Nanowires: Size and Temperature Effects, *Phys. Rev. Lett.* **99**, 226604 (2007).
- [26] Y. Niimi, M. Morota, D. H. Wei, C. Deranlot, M. Basletic, A. Hamzic, A. Fert, and Y. Otani, Extrinsic Spin Hall Effect Induced by Iridium Impurities in Copper, *Phys. Rev. Lett.* **106**, 126601 (2011).
- [27] M. Morota, Y. Niimi, K. Ohnishi, D. H. Wei, T. Tanaka, H. Kontani, T. Kimura, and Y. Otani, Indication of intrinsic spin Hall effect in 4d and 5d transition metals, *Phys. Rev. B* **83**, 174405 (2011).
- [28] S. Takahashi and S. Maekawa, Spin injection and detection in magnetic nanostructures, *Phys. Rev. B* **67**, 052409 (2003).
- [29] Y. Niimi and Y. Otani, Reciprocal spin hall effects in conductors with strong spin–orbit coupling: a review, *Reports on Progress in Physics* **78**, 124501 (2015).
- [30] D. H. Wei, Y. Niimi, B. Gu, T. Ziman, S. Maekawa, and Y. Otani, The spin hall effect as a probe of nonlinear spin fluctuations, *Nature Communications* **3**, 1058 (2012).
- [31] Y. Ou, D. C. Ralph, and R. A. Buhrman, Strong Enhancement of the Spin Hall Effect by Spin Fluctuations near the Curie Point of Fe_xPt_{1-x} Alloys, *Phys. Rev. Lett.* **120**, 097203 (2018).
- [32] P.-H. Wu, D. Qu, Y.-C. Tu, Y.-Z. Lin, C. L. Chien, and S.-Y. Huang, Exploiting Spin Fluctuations for Enhanced Pure Spin Current, *Phys. Rev. Lett.* **128**, 227203 (2022).
- [33] C. Fang, C. Wan, X. Zhang, S. Okamoto, T. Ma, J. Qin, X. Wang, C. Guo, J. Dong, G. Yu, Z. Wen, N. Tang, S. S. P. Parkin, N. Nagaosa, Y. Lu, and X. Han, Observation of the Fluctuation Spin Hall Effect in a Low-Resistivity Antiferromagnet, *Nano Letters* **23**, 11485 (2023).
- [34] S. Okamoto, T. Egami, and N. Nagaosa, Critical Spin Fluctuation Mechanism for the Spin Hall Effect, *Phys. Rev. Lett.* **123**, 196603 (2019).
- [35] Y. Togawa, Y. Kousaka, K. Inoue, and J.-i. Kishine, Symmetry, Structure, and Dynamics of Monoaxial Chiral Magnets, *Journal of the Physical Society of Japan* **85**, 112001 (2016).
- [36] S. S. P. Parkin and R. H. Friend, 3d transition-metal intercalates of the niobium and tantalum dichalcogenides. I. Magnetic properties, *Philosophical Magazine B* **41**, 65 (1980).
- [37] S. Parkin and R. Friend, Magnetic and transport properties of 3d transition metal intercalates of some group Va transition metal dichalcogenides, *Physica B+C* **99**, 219 (1980).
- [38] T. Moriya and T. Miyadai, Evidence for the helical spin structure due to antisymmetric exchange interaction in Cr_{1/3}NbS₂, *Solid State Communications* **42**, 209 (1982).
- [39] T. Miyadai, K. Kikuchi, H. Kondo, S. Sakka, M. Arai, and Y. Ishikawa, Magnetic Properties of Cr_{1/3}NbS₂, *Journal of the Physical Society of Japan* **52**, 1394 (1983).
- [40] Y. A. Izyumov, Modulated, or long-periodic, magnetic structures of crystals, *Soviet Physics Uspekhi* **27**, 845 (1984).
- [41] Y. Kousaka, Y. Nakao, J. Kishine, M. Akita, K. Inoue, and J. Akimitsu, Chiral helimagnetism in T_{1/3}NbS₂ (T=Cr and Mn), *Nuclear Instruments and Methods in Physics Research Section A: Accelerators, Spectrometers, Detectors and Associated Equipment* **600**, 250 (2009).
- [42] Y. Togawa, T. Koyama, K. Takayanagi, S. Mori, Y. Kousaka, J. Akimitsu, S. Nishihara, K. Inoue, A. S. Ovchinnikov, and J. Kishine, Chiral Magnetic Soliton Lattice on a Chiral Helimagnet, *Phys. Rev. Lett.* **108**,

- 107202 (2012).
- [43] N. J. Ghimire, M. A. McGuire, D. S. Parker, B. Sipos, S. Tang, J.-Q. Yan, B. C. Sales, and D. Mandrus, Magnetic phase transition in single crystals of the chiral helimagnet $\text{Cr}_{1/3}\text{NbS}_2$, *Phys. Rev. B* **87**, 104403 (2013).
 - [44] Y. Togawa, Y. Kousaka, S. Nishihara, K. Inoue, J. Akimitsu, A. S. Ovchinnikov, and J. Kishine, Interlayer Magnetoresistance due to Chiral Soliton Lattice Formation in Hexagonal Chiral Magnet CrNb_3S_6 , *Phys. Rev. Lett.* **111**, 197204 (2013).
 - [45] B. J. Chapman, A. C. Bornstein, N. J. Ghimire, D. Mandrus, and M. Lee, Spin structure of the anisotropic helimagnet $\text{Cr}_{1/3}\text{NbS}_2$ in a magnetic field, *Applied Physics Letters* **105**, 072405 (2014).
 - [46] A. C. Bornstein, B. J. Chapman, N. J. Ghimire, D. G. Mandrus, D. S. Parker, and M. Lee, Out-of-plane spin-orientation dependent magnetotransport properties in the anisotropic helimagnet $\text{Cr}_{1/3}\text{NbS}_2$, *Phys. Rev. B* **91**, 184401 (2015).
 - [47] K. Tsuruta, M. Mito, H. Deguchi, J. Kishine, Y. Kousaka, J. Akimitsu, and K. Inoue, Phase diagram of the chiral magnet $\text{Cr}_{1/3}\text{NbS}_2$ in a magnetic field, *Phys. Rev. B* **93**, 104402 (2016).
 - [48] Y. Kousaka, T. Ogura, J. Jiang, K. Mizutani, S. Iwasaki, J. Akimitsu, and Y. Togawa, An emergence of chiral helimagnetism or ferromagnetism governed by Cr intercalation in a dichalcogenide CrNb_3S_6 , *APL Materials* **10**, 090704 (2022).
 - [49] L. Wang, N. Chepiga, D.-K. Ki, L. Li, F. Li, W. Zhu, Y. Kato, O. S. Ovchinnikova, F. Mila, I. Martin, D. Mandrus, and A. F. Morpurgo, Controlling the Topological Sector of Magnetic Solitons in Exfoliated $\text{Cr}_{1/3}\text{NbS}_2$ Crystals, *Phys. Rev. Lett.* **118**, 257203 (2017).
 - [50] R. J. Elliott, Theory of the Effect of Spin-Orbit Coupling on Magnetic Resonance in Some Semiconductors, *Phys. Rev.* **96**, 266 (1954).
 - [51] Y. Yafet, g Factors and Spin-Lattice Relaxation of Conduction Electrons, *Solid State Physics* **14**, 1 (1963).
 - [52] M. Shinozaki, Y. Masaki, R. Aoki, Y. Togawa, and Y. Kato, Intrinsic hysteresis due to the surface barrier for chiral solitons in monoaxial chiral helimagnets, *Phys. Rev. B* **97**, 214413 (2018).
 - [53] A. O. Leonov, Y. Togawa, T. L. Monchesky, A. N. Bogdanov, J. Kishine, Y. Kousaka, M. Miyagawa, T. Koyama, J. Akimitsu, T. Koyama, K. Harada, S. Mori, D. McGrouther, R. Lamb, M. Krajnak, S. McVitie, R. L. Stamps, and K. Inoue, Chiral Surface Twists and Skyrmion Stability in Nanolayers of Cubic Helimagnets, *Phys. Rev. Lett.* **117**, 087202 (2016).
 - [54] Y. Togawa, T. Koyama, Y. Nishimori, Y. Matsumoto, S. McVitie, D. McGrouther, R. L. Stamps, Y. Kousaka, J. Akimitsu, S. Nishihara, K. Inoue, I. G. Bostrem, V. E. Sinitsyn, A. S. Ovchinnikov, and J. Kishine, Magnetic soliton confinement and discretization effects arising from macroscopic coherence in a chiral spin soliton lattice, *Phys. Rev. B* **92**, 220412 (2015).
 - [55] M. Mito, H. Ohsumi, K. Tsuruta, Y. Kotani, T. Nakamura, Y. Togawa, M. Shinozaki, Y. Kato, J.-i. Kishine, J.-i. Ohe, Y. Kousaka, J. Akimitsu, and K. Inoue, Geometrical protection of topological magnetic solitons in microprocessed chiral magnets, *Phys. Rev. B* **97**, 024408 (2018).
 - [56] H. Isshiki, Z. Zhu, H. Mizuno, R. Uesugi, T. Higo, S. Nakatsuji, and Y. Otani, Determination of spin Hall angle in the Weyl ferromagnet Co_2MnGa by taking into account the thermoelectric contributions, *Phys. Rev. Mater.* **6**, 084411 (2022).
 - [57] J. L. García-Palacios and F. J. Lázaro, Langevin-dynamics study of the dynamical properties of small magnetic particles, *Phys. Rev. B* **58**, 14937 (1998).
 - [58] K. Momma and F. Izumi, VESTA 3 for three-dimensional visualization of crystal, volumetric and morphology data, *Journal of Applied Crystallography* **44**, 1272 (2011).

METHODS

Device fabrication

CrNb₃S₆ single crystals were grown by the chemical transport method, as described elsewhere [41]. CrNb₃S₆ thin flakes were obtained by the conventional mechanical exfoliation method using Nitto tapes. These thin flakes were transferred onto a SiO₂ (285 nm)/Si substrate. The exfoliation process was performed inside a glove box filled with Ar gas of 99.9999% purity to prevent oxidation of the CrNb₃S₆ thin flakes.

The spin valve structure was fabricated using a conventional lift-off method. Two Py wires and a Cu bridge were patterned by electron beam lithography onto the substrate coated with polymethyl-methacrylate (PMMA) resist for the deposition of Py and Cu. A pair of Py wires was first deposited on both sides of the CrNb₃S₆ thin flake using an electron beam evaporator. The width and thickness of the Py wires are 100 and 30 nm, respectively. Before the deposition of the Cu bridge, Ar ion beam milling was performed for approximately 1 minute to remove the residual resist and clean the surfaces of the Py wires and CrNb₃S₆ thin flakes. After the Ar ion beam milling, the device was transferred to another chamber without breaking vacuum, and the Cu bridge was deposited by a Joule heating evaporator. The width of the Cu bridge is 100 nm, and the thickness is either 100 or 200 nm. The width of the CrNb₃S₆ thin flakes is approximately 400 nm, and the thickness t of the CrNb₃S₆ thin flakes used in this work is 43 nm, 50 nm, 52 nm, 72 nm and 73 nm (see Extended Data Table 1). We also fabricated lateral spin valve devices without CrNb₃S₆ flakes as reference devices to evaluate the spin diffusion length. The device structure, such as the width and thickness of the Py and Cu wires, is the same as that of the devices with CrNb₃S₆.

Measurement set-up

The nonlocal spin valve and inverse spin Hall effect measurements were conducted using an ac lock-in amplifier and a ⁴He flow cryostat. A magnetic field in the range of ± 0.4 T was applied to the device using an electromagnet.

Details of micromagnetic simulations

To verify the magnetic field dependence of R_{S2} , we performed numerical simulations of the magnetic structure of a chiral helimagnet under an applied magnetic field. We employed the classical Heisenberg spin system with

the following Hamiltonian:

$$\mathcal{H} = - \sum_{\langle i,j \rangle} J \vec{S}_i \cdot \vec{S}_j + \sum_{\langle i,j' \rangle} \vec{D} \cdot (\vec{S}_i \times \vec{S}_{j'}) + \sum_i K_z S_{iz}^2, \quad (1)$$

where \vec{S}_i is the spin of the i site. J and $\vec{D} = (0, 0, D)$ represent the ferromagnetic exchange interaction and the DM interaction. We use the 2-dimensional spin system consists of $L_z \times 10$ spins, where L_z is the system length corresponds to thickness in the experiments. $\langle i, j \rangle$ takes nearest neighbor sites whereas $\langle i, j' \rangle$ takes nearest neighbor sites only in the z direction. K_z is the anisotropy energy along the hard z -axis, which stabilizes the helical spin structure with a propagation vector along the z -axis.

Using the Landau-Lifshitz-Gilbert equation, we numerically calculated the magnetic structure under a magnetic field applied parallel to the y -axis (parallel to the helical plane). The values of J and D were both set to 6.2 meV resulting in a helical magnetic structure with a period (L_0) of approximately 13.3 spins in the 2-dimensional system. Additionally, thermal fluctuations of 10 K were incorporated by introducing a random magnetic field [57]. We set the $K_z = 6.2 \times 10^{-2}$ meV that is enough small compared with J and D .

DATA AVAILABILITY

Data are available from the corresponding authors upon request.

ACKNOWLEDGMENTS

The authors thank J. Kishine, S. Maekawa, and S. Okumura for fruitful discussions. The crystal structure of CrNb₃S₆ was visualized using VESTA [58]. This work was supported by JSPS KAKENHI (Grant Nos. JP22H04481, JP23H00257, JP23K13062, JP23H00091, JP23H01870), JST FOREST (Grant No. JPMJFR2134), and the Cooperative Research Project of RIEC, Tohoku University.

AUTHOR CONTRIBUTIONS

N.J., S.S., I.S., K.Y., and R.K. performed the device fabrication and measurements. Y.S., H.S., Y.K., and Y.T. synthesized the CrNb₃S₆ crystals. J.O. conducted the micromagnetic simulations. N.J. wrote the manuscript with input from S.T., J.O., Y.T., and Y.N.

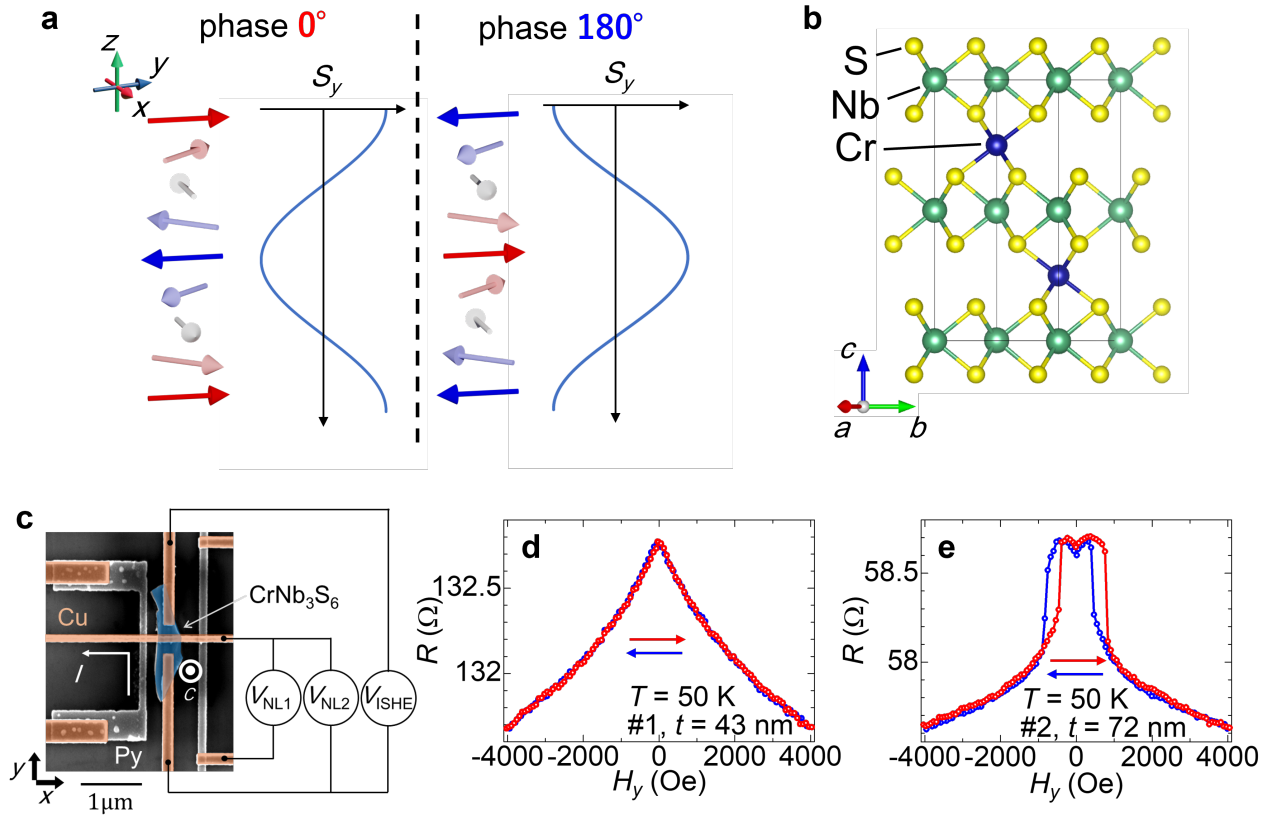


FIG. 1 | Basic properties of CrNb₃S₆. **a**, Definition of the spin phase in a helical magnetic structure. The 0° and 180° phases are defined when the surface magnetic moment is parallel and antiparallel to an in-plane reference axis (taken here as the y -axis), respectively. **b**, Crystal structure of CrNb₃S₆. The black solid line represents a unit cell. **c**, A scanning electron microscope image of a typical nonlocal spin valve (NLSV) device. The scale bar is 1 μm. **d**, **e**, Magnetoresistance of CrNb₃S₆ with thicknesses of 43 nm (**d**) and 72 nm (**e**) measured at 50 K. The red and blue data correspond to the magnetic field increasing and decreasing processes, respectively.

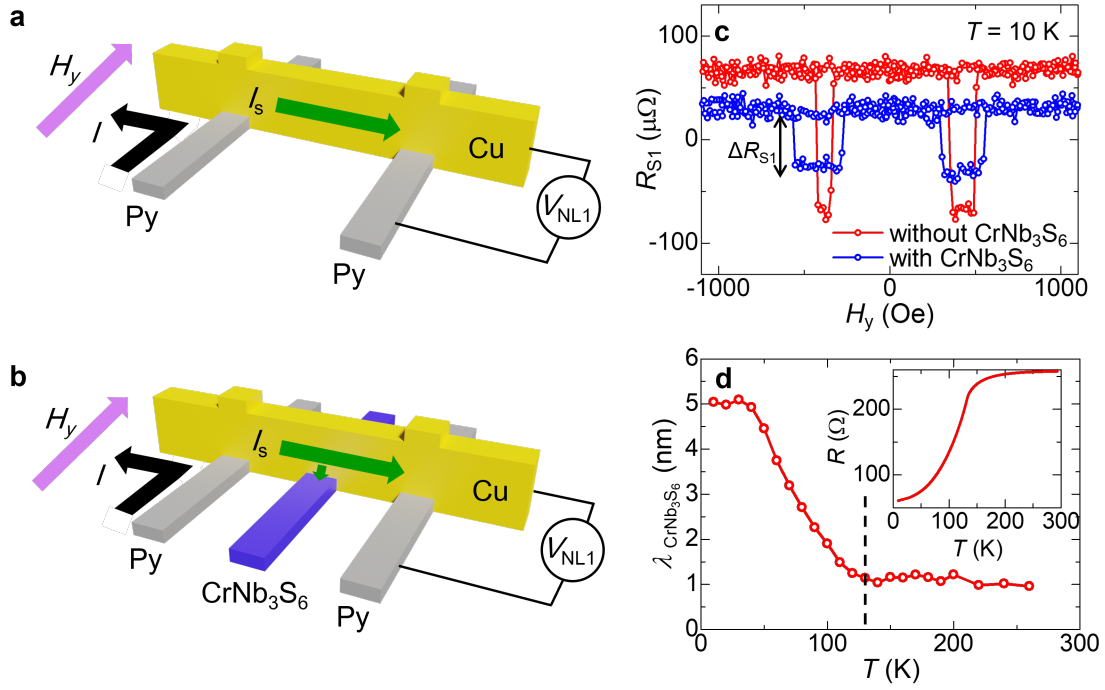


FIG. 2 | **Determination of spin diffusion length of CrNb₃S₆.** **a, b**, Schematic illustrations of NLSV measurements without (**a**) and with (**b**) an insertion of a CrNb₃S₆ flake. **c**, NLSV signal R_{S1} with (blue) and without (red) a 30 nm thick CrNb₃S₆ flake measured at $T = 10$ K. **d**, Spin diffusion length of the CrNb₃S₆ flake as a function of temperature. The inset shows the temperature dependence of the resistance R of the CrNb₃S₆ flake.

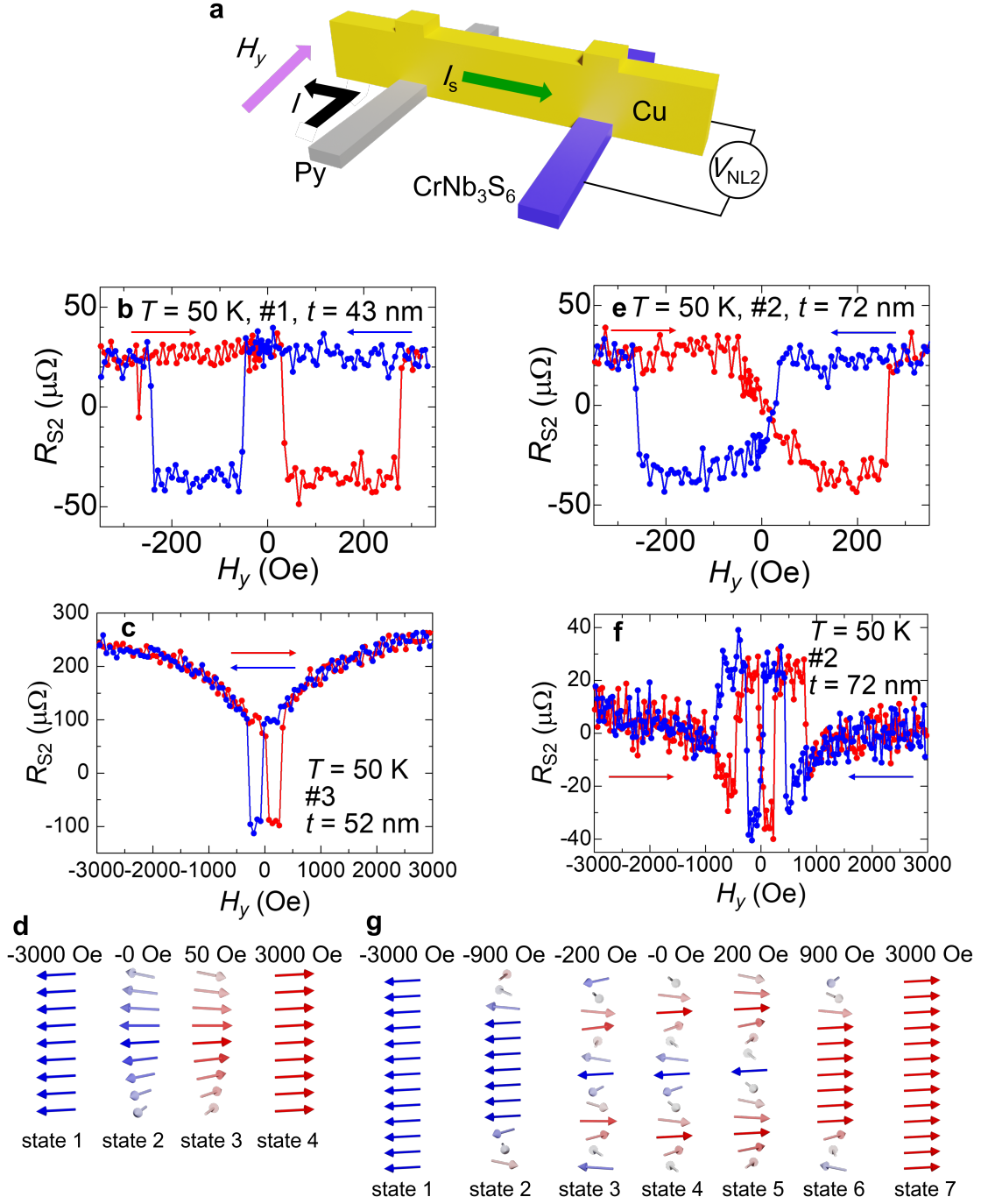


FIG. 3| Spin phase detection in CrNb₃S₆ flakes. **a**, A schematic illustration of the spin phase detection measurement. **b**, **c**, NLSV signal R_{S2} at $T = 50$ K using a 43 nm ($\approx L_0$) thick CrNb₃S₆ flake for a low magnetic field region (**b**) and a 52 nm ($\approx L_0$) thick CrNb₃S₆ flake for a high magnetic field region (**c**). **d**, The expected magnetic structures at characteristic magnetic fields during the magnetic field increasing process for the $t \approx L_0$ thick CrNb₃S₆ flake. **e**, **f**, NLSV signal R_{S2} at $T = 50$ K using a 72 nm ($\approx 1.5L_0$) thick CrNb₃S₆ flake for a low magnetic field region (**e**) and a high magnetic field region (**f**). **g**, The expected magnetic structures at characteristic magnetic fields during the magnetic field increasing process for the $t \approx 1.5L_0$ thick CrNb₃S₆ flake.

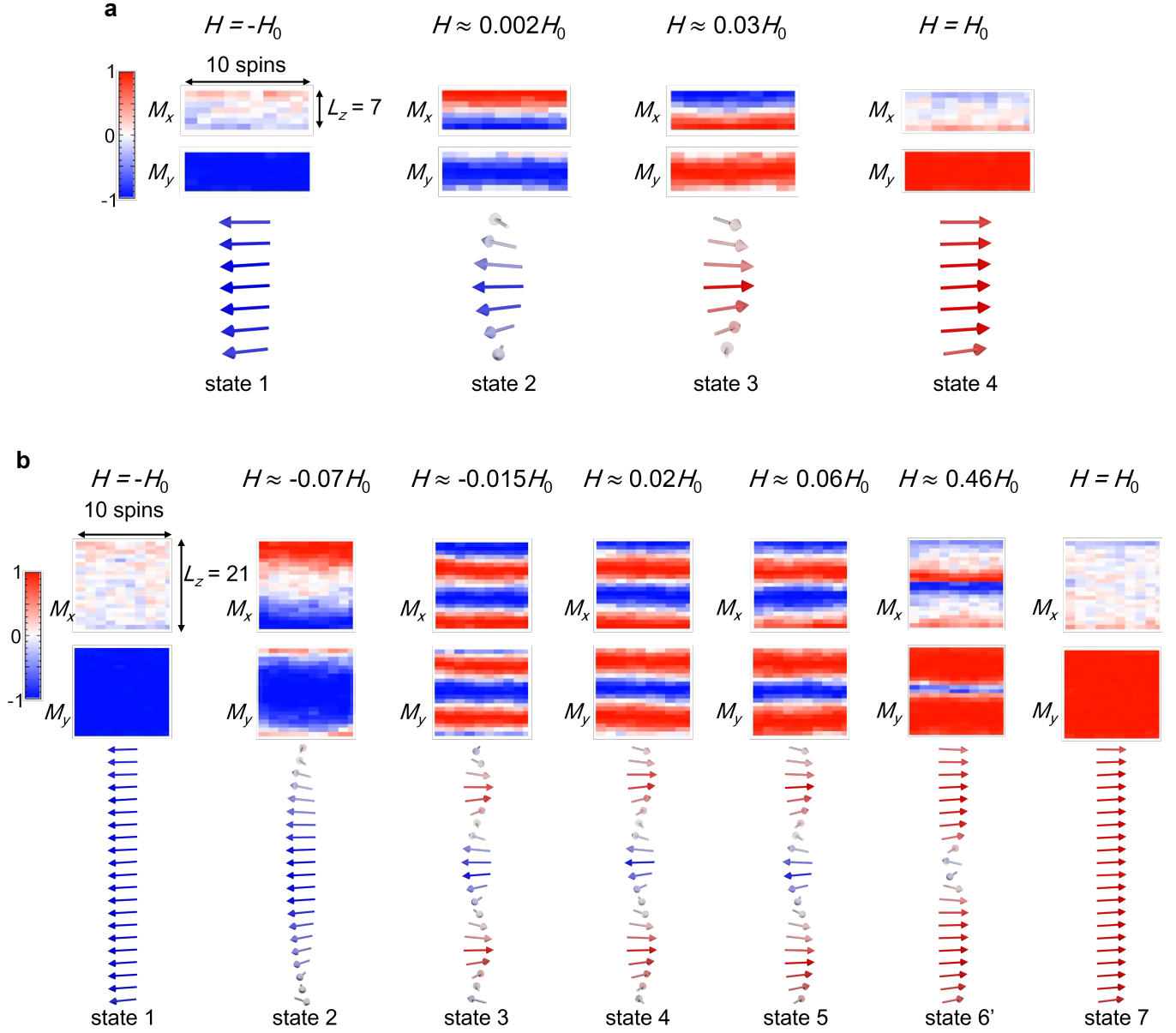


FIG. 4| Micromagnetic simulations. **a**, Snapshots of the magnetization components along the x - and y -directions (M_x and M_y , respectively) and magnetic structure averaged over 10 spins at characteristic magnetic fields during the field-increasing process for a $L_z = 7$ ($\approx 0.5L_0$) helimagnet. The maximum values of M_x and M_y are normalized to 1. **b**, Snapshots of M_x and M_y and magnetic structure averaged over 10 spins at characteristic magnetic fields during the field-increasing process for a $L_z = 21$ ($\approx 1.5L_0$) helimagnet. The maximum values of M_x and M_y are normalized to 1.

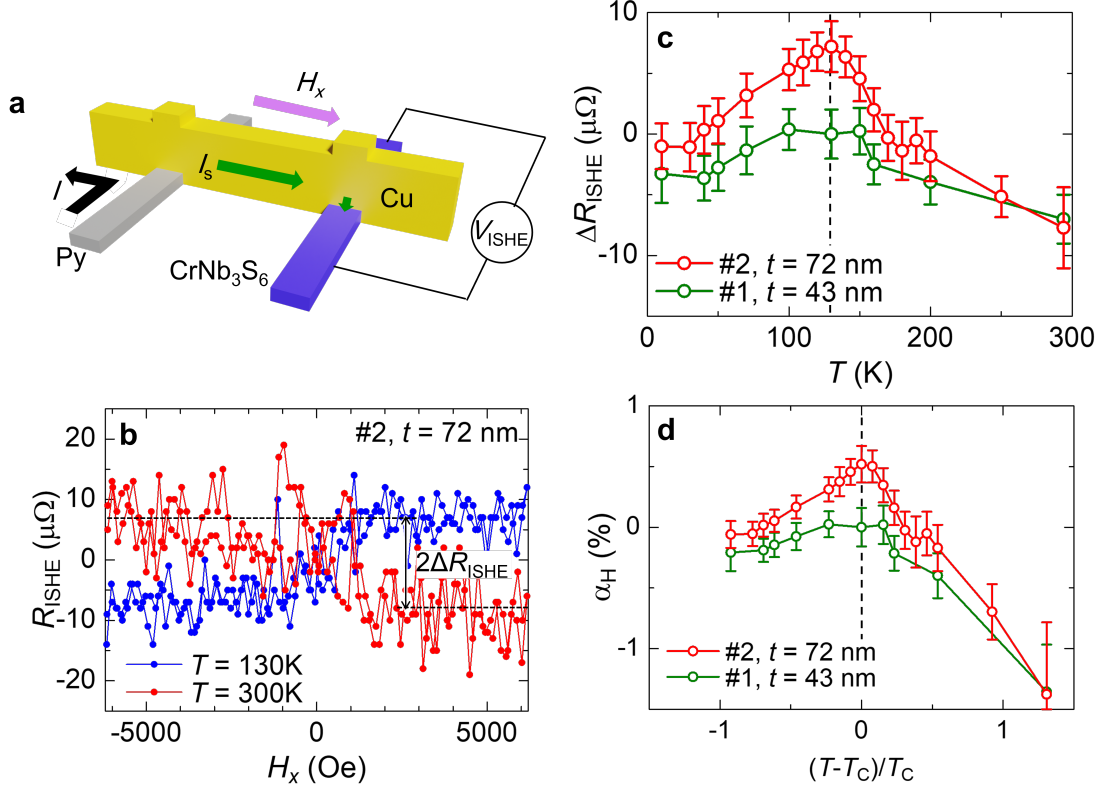
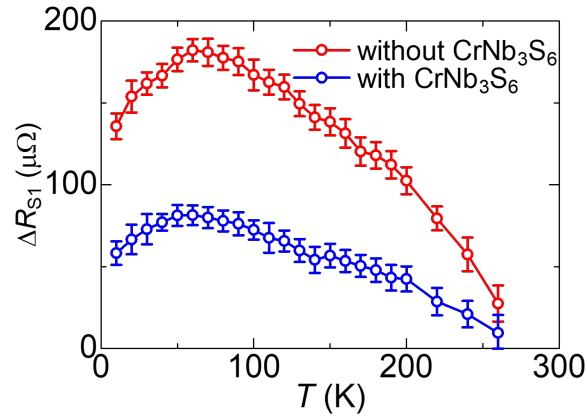


FIG. 5 | Inverse spin Hall effect measurements in CrNb₃S₆ flakes. **a**, A schematic illustration of the ISHE measurement. **b**, R_{ISHE} of a 72 nm-thick CrNb₃S₆ device measured at $T = 130$ and 300 K . ΔR_{ISHE} is defined in the figure. **c**, Temperature dependence of ΔR_{ISHE} for $t = 43$ and 72 nm thick CrNb₃S₆ devices. **d**, The spin Hall angle α_H as a function of the reduced temperature, $(T - T_C)/T_C$, for $t = 43$ and 72 nm thick CrNb₃S₆ devices.

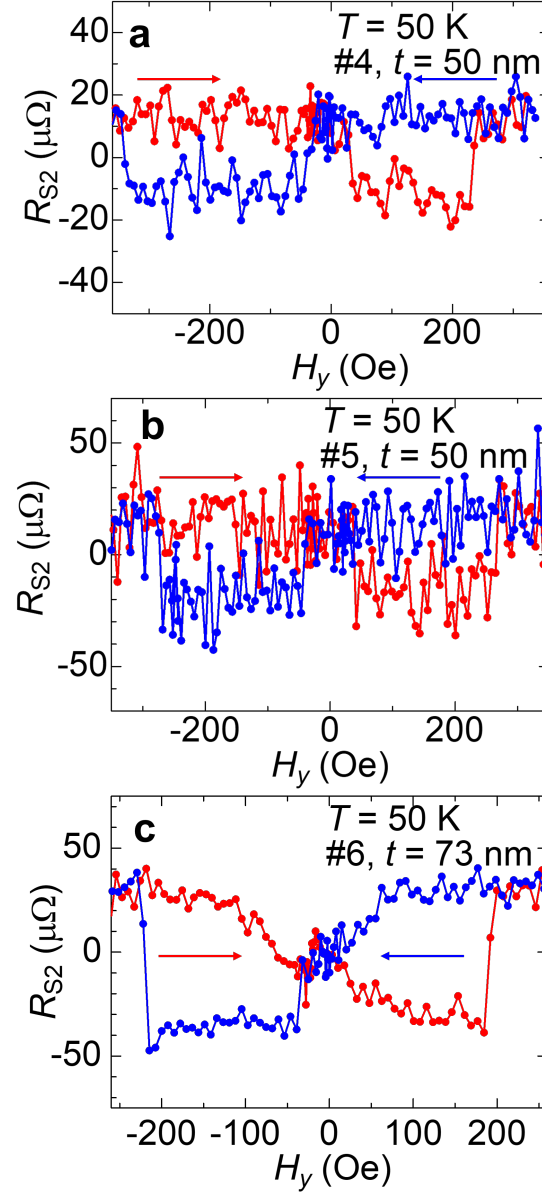
EXTENDED DATA

Sample No.	Thickness (nm)	Spin Signal	Spin Hall
1	43 ($\approx L_0$)	✓	✓
2	72 ($\approx 1.5L_0$)	✓	✓
3	52 ($\approx L_0$)	✓	✓
4	50 ($\approx L_0$)	✓	✓
5	50 ($\approx L_0$)	✓	
6	73 ($\approx 1.5L_0$)	✓	✓

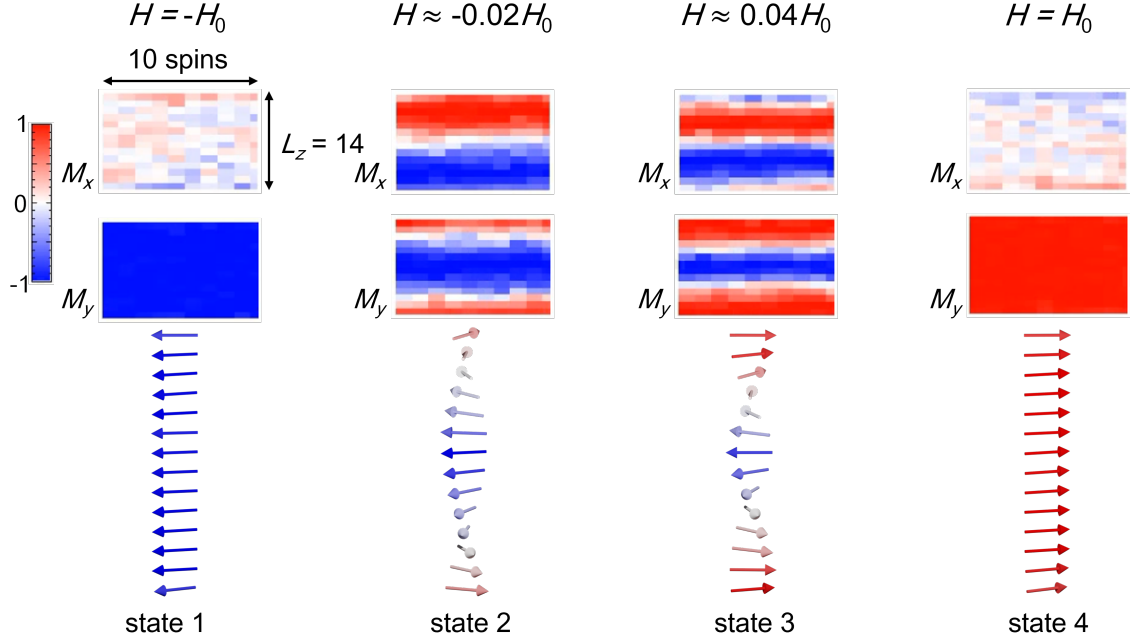
Extended Data Table 1 Thickness of the measured samples and the corresponding measurements performed.



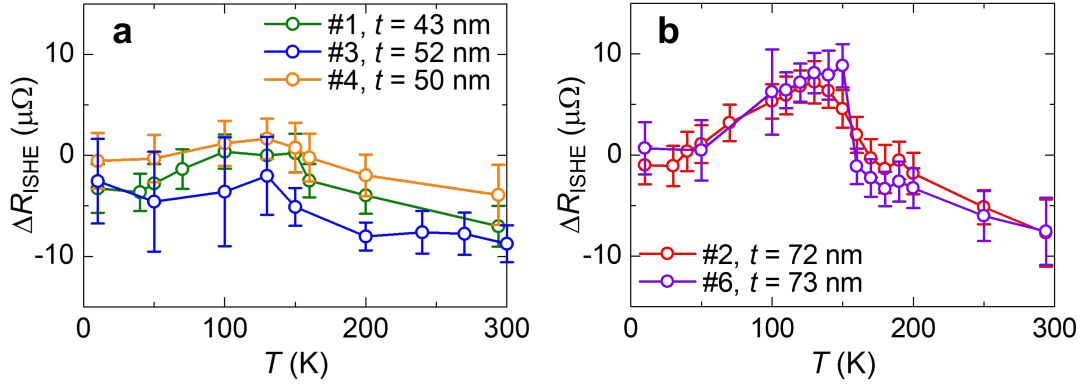
Extended Data Fig. 1 | Temperature dependence of the NLSV signal with and without a 30 nm thick CrNb_3S_6 flake. The temperature dependence of ΔR_{S1} for devices with and without the CrNb_3S_6 flake.



Extended Data Fig. 2| Reproducibility of the NLSV signal using CrNb_3S_6 flakes. NLSV signals R_{S2} at $T = 50$ K using $t \approx L_0$ (a, b) and $t \approx 1.5L_0$ (c) CrNb_3S_6 flakes.



Extended Data Fig. 3| Micromagnetic simulations for a $L_z = 14 (\approx L_0)$ helimagnet. Snapshots of the magnetization components along the x - and y -directions (M_x and M_y , respectively) and magnetic structure averaged over 10 spins at characteristic magnetic fields during the field-increasing process for a $L_z = 14 (\approx L_0)$ helimagnet. The maximum values of M_x and M_y are normalized to 1.



Extended Data Fig. 4| Reproducibility of inverse spin Hall effect. Temperature dependence of ΔR_{ISHE} for $t \approx L_0$ (a) and $t \approx 1.5L_0$ (b) CrNb_3S_6 devices. The data for sample #1 and #2 are the same as those shown in the main text.